ACS APPLIED MATERIALS & INTERFACES

Research Article

www.acsami.org

In Vitro Model of a Fibrosa Layer of a Heart Valve

Soumen Jana,[†] Amir Lerman,*[,†] and Robert D Simari*[,‡]

[†]Division of Cardiovascular Diseases, Mayo Clinic, 200 First Street SW, Rochester, Minnesota 55905, United States

[‡]School of Medicine, University of Kansas, 3901 Rainbow Boulevard, Kansas City, Kansas 66160, United States

Supporting Information

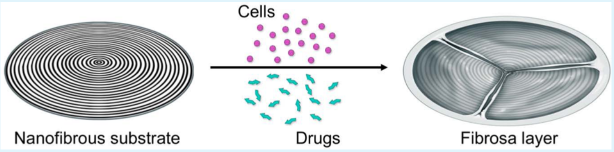

ABSTRACT: The fibrosa layer of a cardiac aortic valve is composed mostly of a dense network of type I collagen fibers oriented in circumferential direction. This main layer bears the tensile load and responds to the high stress on a leaflet. The inner fibrosa layer is also the site of pathophysiologic changes that result in valvular dysfunction, including stenosis and regurgitation. In vitro studies of these changes are limited by the absence of a substrate that mimics the circumferentially oriented structure of the fibrosa layer. In heart valve tissue engineering, generation of this layer is challenging. This study aimed to develop an artificial fibrosa layer of a native aortic leaflet. A unique morphologically biomimicked, pliable, but standalone substrate with circumferentially oriented nanofibers was fabricated by electrospinning on a novel collector designed for this study. The substrate had low-bulk tensile stiffness and ultimate strength; thus, cultured valvular interstitial cells (VICs) showed a fibroblast phenotype that is generally observed in a healthy aortic leaflet. Furthermore, gene and protein expression and morphology of VICs in substrates were close to those in the fibrosa layer of a native aortic leaflet. This artificial fibrosa layer can be useful for in vitro studies of valvular dysfunctions.

KEYWORDS: *cardiac valve, fibrosa layer, nanofibrous substrate, tissue engineering, valvular interstitial cells*

■ INTRODUCTION

According to WHO estimates, cardiovascular diseases (CVD) are the primary cause of human mortality and morbidity worldwide.[1,2] Among them, cardiac valve degeneration compromises valve integrity, resulting in stenotic or incompetent valves.[3,4] This degeneration tends to occur primarily in the fibrosa layer—the subendothelial aortic side of the leaflet—consisting mainly of circumferentially arranged collagen fibrils parallel to the leaflet margin with the primary cellular element comprising fibroblasts known as valvular interstitial cells (VICs).[5,6] Multiple factors including adverse biochemical factors and mechanical stresses are associated with this degeneration.[7,8] In addition to VICs, valvular endothelial cells (VECs) are exposed to these biochemical factors and mechanical stresses leading to their degeneration. The degenerated VECs indirectly cause calcification by activating the VICs or triggering the VICs to change to osteoblast-like VICs.[9,10] In mature heart valve, VECs can trans-differentiate to mesenchymal phenotype in the presence of transformation growth factor—β (TGF-β)—which further recruits transformed mesenchymal stem cells in osteogenic calcification.[11,12]

Similarly, in response to TGF-β, valvular precursor cells undergo transition to VIC-like cells, which may cause calcification depending on the valvular condition.[10]

In heart valve tissue engineering, development of a fibrosa layer is critical as it is the main tensile load bearer and responsible for a high-stress response of a leaflet.[13] On a substrate without appropriate physical and mechanical properties, the phenotype of VICs could be changed from quiescent fibroblast to active myofibroblast and then to pathogenic myofibroblast. Further, investigations of leaflet degeneration are primarily performed in vitro, mostly in tissue culture plate (TCP) because of limited in vivo resources. However, regardless of their healthy or diseased valve sources, VICs on TCP show the pathogenic myofibroblast phenotype because of high stiffness of substrate.[14] Thus, without a substrate with appropriate structural and mechanical properties comparable to that of a native fibrosa layer, valve dysfunction investigations cannot be worthwhile.

Studies aimed at developing a biomimicked substrate of a native fibrosa layer could generate model fibrosa layers. In designing the substrate, we considered three issues: (1) the bulk stiffness and strength of the substrate should be as low as possible and lower than the corresponding bulk stiffness and strength of a native leaflet to maintain the fibroblast phenotype of VICs, (2) the substrate should be made of nanofibers to mimic the fibril morphology of collagen, the main component of a fibrosa layer, and (3) orientation of nanofibers in the substrate should be circumferential, mimicking the collagen fibril orientation in a fibrosa layer. It is expected that culturing VICs in the biomimicked substrate will produce a prototype of a native fibrosa layer suitable for valve dysfunction investigations.

To generate an appropriate in vitro fibrosa layer model, we prepared circumferentially oriented nanofibrous (CON) substrate by electrospinning polycaprolactone (PCL), an FDA

Received: June 4, 2015
Accepted: August 21, 2015
Published: August 21, 2015

DOI: 10.1021/acsami.5b04805
ACS Appl. Mater. Interfaces 2015, 7, 20012−20020

approved bioresorbable and biocompatible semicrystalline linear aliphatic polyester commonly used in biomedical application, including tissue engineering.[15−17] PCL degrades through hydrolysis of its aliphatic ester linkage and the degradation products are not generally toxic.[18] PCL was selected because it is easy to spin, has a slow biodegradation property and can be applied for an in vivo study. Nanofibers made of PCL can bear the load of transvalvular pressure (~8 kPa).[19,20] Because of its slow degradation (depending on its molecular weight), seeding cell may have enough time to grow and deposit extracellular matrices slowly in vitro.[21] A randomly oriented nanofibrous (RON) substrate made of PCL was used to compare the influence of fiber orientation from a CON substrate on VICs. A TCP well plate was used as a control. VICs from porcine aortic valve (PAV) leaflet were seeded and then cultured on these substrates for 1 month and their morphological and biological results were compared to those in the fibrosa layer of PAV leaflets.

RESULTS AND DISCUSSION

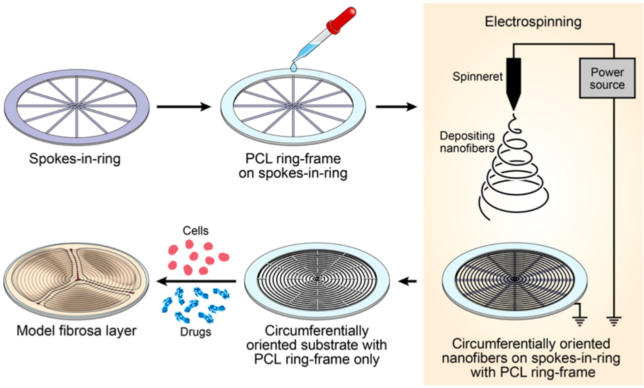

Figure 1. Schematic diagram explaining the fabrication process of a model fibrosa layer (from left in a clockwise direction). A novel spokes-in-ring collector. Fabricating an ~0.25 mm thick layer of PCL ring-frame on the collector. Electrospinning circumferentially oriented nanofibers on the collector with an attached PCL ring-frame. Circumferentially oriented nanofibrous substrate containing oriented nanofibers and PCL ring-frame. Generation of a model fibrosa layer after culturing cells on the circumferentially oriented nanofibrous substrate in the presence of growth factors.

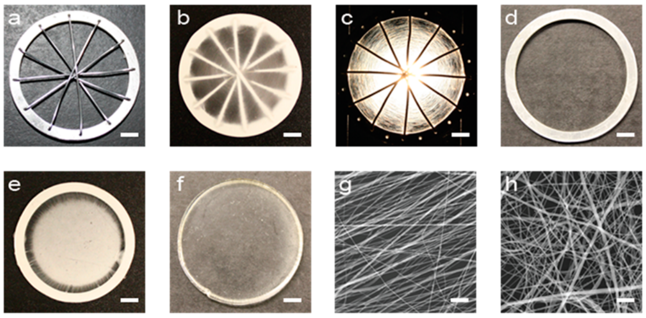

Figure 2. Fabricated substrates and their characteristics. (a) Photograph of a spokes-in-ring collector made of aluminum, scale: 5 mm. (b) Photograph of a spokes-in-ring-shaped CON substrate with circumferentially oriented PCL nanofibers connected to adjacent nanofibrous spokes, scale: 5 mm. (c) Photograph of circumferentially oriented PCL nanofibers in a CON substrate against a light backdrop, scale 5 mm. The sample is placed against a bright light in a dark room to see the fiber orientation in the sample. (d) Photograph of an aluminum ring collector to produce a randomly oriented nanofibrous substrate, scale: 6 mm. (e) Photograph of a ring-shaped RON substrate with randomly oriented PCL nanofibers in the inner space of the ring, scale: 5 mm. (f) Disc (WPD substrate) cut from a well of a 6-well polystyrene tissue culture plate, scale 5 mm. (g) A SEM image of circumferentially oriented PCL nanofibers in a CON substrate, scale 6 μm. (h) SEM image of randomly oriented PCL nanofibers in a RON substrate, scale 6 μm.

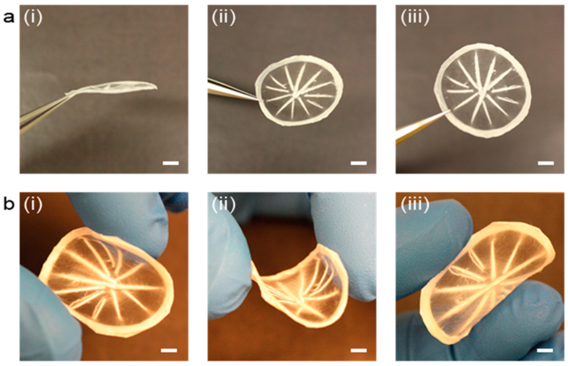

Figure 3. Standalone and pliable CON substrate. (a) CON substrates shown at different angles are standalone as they do not require any structural support, scales: (i) 4.7 mm, (ii) 5.1 mm, and (iii) 4.5 mm. (b) CON substrates shown at different angles are pliable; scales: (i) 3.4 mm, (ii) 3.2 mm, and (iii) 3.0 mm.

Among techniques including phase separation and self-assembly, electrospinning is the most commonly used to prepare nanofibrous substrates because of its versatility, applicability to most polymers, easy handling, and cost-effectiveness.[15−17] In this technique, orientation of the deposited fibers depends on the fiber-collector design. The fabrication process of a model fibrosa layer consists of several steps shown in Figure 1. We first designed a novel spokes-in-ring collector to fabricate circumferentially oriented nanofibers (Figure 2a). An ~0.25 mm thick PCL ring-frame was made on one side of the ring periphery of the collector by pouring 18 wt % PCL solution. We then produced a CON substrate by electrospinning 9 wt % PCL solution on the collector. Between the spokes, a magnetic field formed that pulled one end of a nanofiber toward one spoke and another end toward the adjacent spoke perpendicularly; thus, deposited fibers were concentric. The developed substrates have a spokes-in-ring shape with circumferentially oriented PCL nanofibers connected to adjacent nanofibrous spokes (Figures 2b, c and Figure S1). The nanofibrous membrane together with the PCL ring-frame at its periphery can be detached easily from the collector. Unlike other generally used nanofibrous substrates in tissue engineering, our developed CON substrates do not require structural support such as glass coverslip at their back because of presence of the PCL ring-frame at their peripheries, so these substrates are fully standalone (Figure 3a). Presence of glass coverslip (stiffness: 72.4 GPa), which is stiffer than a polystyrene tissue culture plate (stiffness: 3 GPa), will certainly change the phenotype of VICs from fibroblast to pathogenic myofibroblast, which is not desirable at all.[14] Further, the CON substrates are pliable (Figure 3b). We hypothesized that this CON substrate can be a prototype of a native fibrosa layer after culturing the substrate with VICs. On an aluminum ring with a PCL ring-frame on it (Figure 2d), we prepared a RON substrate as a control substrate (Figure 2e). A metal plate was placed at the back of the ring to produce random nanofibers in the inner space of the ring. Discs (polystyrene well plate disc, WPD) with diameters similar to a CON or RON substrate were cut from the wells of 6-well tissue culture plates to serve as another control (Figure 2f). Comparisons of substrates and their VIC-cultured counterparts were made with freshly isolated PAV leaflets.

The structure of collectors influences the porosity of substrates and CON substrate had much higher porosity compared to RON (Figures 2g, h). Because of the non-conductive property of deposited polymeric (PCL) nanofibers in electrospinning system, the fibers hold a charge. In our spokes-in-ring collector, only two ends of nanofibers were attached to adjacent spokes. Fibers between two adjacent spokes thus carried similar charges, causing repulsion among the adjacent fibers leading to high porosity in CON substrate. Unlike CON substrate, nanofibers in RON substrate were compact because of the presence of a metallic plate at the back of the ring collector while electrospinning. However, we prepared a thin RON substrate so that cells can spread into the substrate.

The fiber diameter of both CON and RON substrates scanned in electron microscopy was 370 ± 73 nm (Figures 2g, h). For tensile test, a third of the CON and RON substrates with a shape equivalent to the shape of a PAV leaflet served as the test sample. The stress−strain curves were almost linear until they reached ultimate strength point, and stiffness of the substrates was calculated from the linear region. The uniaxial bulk tensile moduli of CON and RON substrates were 0.33 ± 0.19 MPa and 3.82 ± 1.03 MPa, respectively, and their ultimate strengths were 0.14 ± 0.06 MPa and 1.21 ± 0.39 MPa, respectively. For aortic valve leaflet and WPD, tensile moduli were 7.25 ± 2.10 MPa and ~3 GPa and tensile ultimate strengths were 1.83 ± 0.64 MPa and ~40 MPa, respectively.[22−24] Among all the substrates, the CON substrate was significantly lower ($p < 0.01$ by ANOVA) in terms of stiffness and ultimate strength.

High porosity contributed low bulk tensile modulus to CON substrates. Beside high porosity, circumferential orientation of fibers in a CON substrate was responsible for its low bulk mechanical properties. A third of a CON substrate (Figure 4a, a schematic diagram) has almost equivalent shape and circumferential orientation of a fibrosa layer in a PAV leaflet. When a tensile load T is applied to this leaflet-shaped CON substrate in the circumferential direction, circumferentially oriented nanofibers across the substrate bear the load. One component of T (cosine of T) tangent to nanofibers will be responsible for elongating the fibers; another component of T (sine of T) perpendicular to nanofibers will be responsible for straightening the fibers (Figures 4b, c). With this low force ($T\cos\alpha$ or $T\cos\beta < T$), fibers will elongate slowly first with the elongation of small polymer chains in the fibers and then comparatively longer chains so the fibers will have high elongation. If the nanofibers are straight instead of circumferentially oriented, the nanofibers will bear the full load T instead of its component for their elongation. With full load T, small polymer chains in the fibers will have less chance to resist the load compared to their longer counterparts and less elongation of fibers will occur, i.e., high stiffness will be observed. The stiffness of the PCL nanofibrous substrate was 22.08 ± 5.19 MPa when the aligned fibers in the substrate were straight.

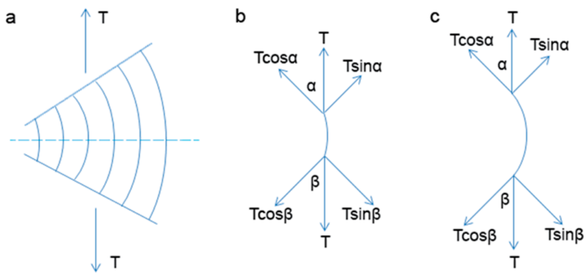

Figure 4. Force resolution of a tensile load on a CON substrate. (a) Schematic of a third of a CON substrate under tensile load *T*. (b) Force resolution of tensile load *T* on a circumferentially oriented short nanofiber of the CON substrate. (c) Force resolution of tensile load *T* on a circumferentially oriented long nanofiber of the CON substrate.

Furthermore, lengths of all the circumferentially oriented nanofibers across the substrate are not similar and shorter nanofibers will face more strain compared to longer ones for the same load. Thus, straightening with elongation and then rupture will occur to the shorter nanofibers first and will propagate toward comparatively longer nanofibers. As all fibers do not work together equally at any time against the load, a low amount of load will be required to rupture the whole sample; thus, CON substrates showed low stiffness and strength with high elongation. In this schematic image of a leaflet-shaped CON substrate (Figure 4a), only fibers within two consecutive spokes have been considered to keep the analysis simple. However, for fibers with more spokes (a dashed line, Figure 4a), a similar explanation can be adopted. Fibers at different fiber−spoke junctions will face equivalent force components but in different directions. Therefore, fibers within same consecutive spokes and within different consecutive spokes will face varied strain. Seeded VICs will witness similar force resolutions when they stretch themselves during their growth. In case of RON substrates, the fibers were randomly oriented and can be considered homogeneous in the tensile testing plane. Consequently, all the fibers in a RON substrate will resist together uniformly at any point of tensile testing. Because of the compactness of fibers in RON substrates, the substrates showed higher mechanical properties compared to CON substrates. Biaxial tensile tests that are generally applied to a trilayered leaflet to measure its mechanical properties were not applicable to the CON substrate as it could not bear load in the direction normal to circumferentially oriented fibers.[25] The goal of this study was to keep the bulk stiffness of the substrate as low as possible to avoid contractile myofibroblast phenotype (mainly responsible for stenosis and regurgitation of a heart valve)[26] of VICs on the substrate.[27] A tissue-engineered, transvalvular load-bearing tubular valve made of fibroblast-deposited collagen showed contraction after reaching to maturity possibly owing to lack of appropriate microenvironment including influence of morphology during development.[28] In this respect, morphology-induced manifestation of VICs was investigated in this study and further, the CON substrate could not be applied in native dynamic environment because of its very low bulk stiffness in radial direction and high pore size.

VICs harvested from PAV leaflets were seeded (100 000 cells per substrate or ~20 000 per cm^2) on CON, RON, and WPD substrates and cultured for one month in the presence of ascorbic acid, which was used to induce the deposition of collagen, the main component of a native leaflet. Fewer cells were seeded to avoid cell−cell contact at the beginning of cell culture and to engage the influence of morphology of substrates on seeded cells. The proliferation of VICs was the highest on CON substrate and lowest on WPD substrate (Figure 5a), which confirms that nanofibrous substrate supports proliferation of VICs, and oriented nanofibers favor higher proliferation of VICs. In fetal valves, VIC density, proliferation and apoptosis are higher than in adult valves.[29] This reported message in conjunction with above proliferation results conveys that CON substrates provided more favorable environment for higher growth of VICs compared other substrates. After one month of culturing, VICs on the CON substrates were stretched, smoothed flat, and aligned concentrically with almost no empty space between the adjacent cells (Figure 5b); whereas the same VICs on RON substrates were less stretched, more irregular, and randomly oriented with empty space between the adjacent cells (Figure 5c). VICs on the WPD substrates were spindle-shaped and showed sporadic radial orientation. Very few cells were stretched and many gaps between these cells on the WPD substrates were observed (Figure 5d). Both morphologies and mechanical properties of the substrates played crucial roles in determining the behaviors of VICs, their shapes, orientation, and cell-to-cell connectivity. Through SEM imaging, cells were observed at both sides of CON and RON substrates only, possibly because of high porosity and stand-alone structure of the nanofibrous substrates.

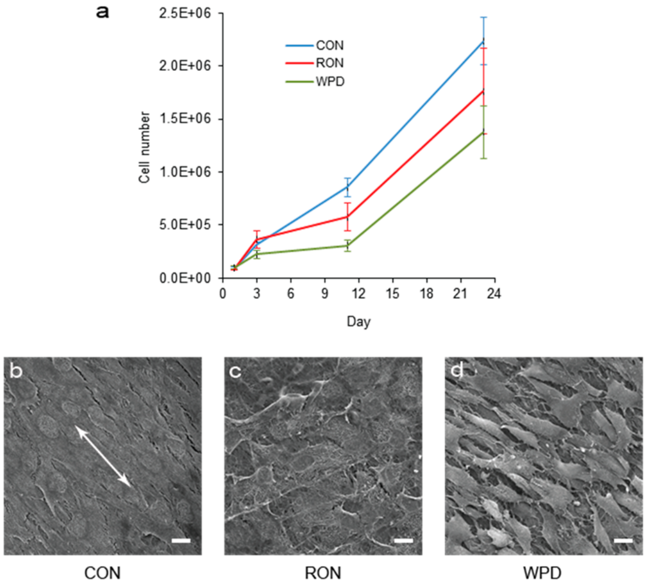

Figure 5. Proliferation study and characteristics of cultured VICs on substrates. (a) The proliferation study of VICs on CON, RON, and WPD substrates was conducted at 3-, 12-, and 24-day time points. The highest proliferation was observed on the CON substrate and lowest on the WPD substrate. (b) SEM image of aligned, flat and stretched VICS with almost no empty space between the cells on a CON substrate, scale 13 μm. White arrow shows the fiber orientation. (c) SEM image of unevenly flat and randomly oriented VICs on a RON substrate, scale 13 μm. (d) SEM image of spindle shaped and radially oriented VICs on a WPD substrate, scale 13 μm.

We also observed deposition of collagen fibrils from VICs on each type of substrate. The fibrils on CON substrates were mostly aligned, similar to aligned collagen fibrils in a native fibrosa layer (Figures 6a, b), whereas no alignments occurred on RON substrates (Figure 6c). On WPD substrates, the fibrils were sparsely aligned (Figure 6d). Masson's trichrome staining[30] confirmed the collagen nature of fibrils (Figures 6e−h). From the top surface, only WPD substrates showed more than one cell layer with different cell orientations. Similarly, CON or RON substrates had layers of VICs throughout the substrates (Figure S2). The diameters of collagen fibrils on all substrates were almost half of those in a native aortic fibrosa layer (50 ± 0.834 nm); their diameters on CON, RON, and WPD substrates were 25.6 ± 0.9, 24.1 ± 0.7, and 22.6 ± 0.3 nm, respectively. The collagen fibril diameter on WPD substrate was significantly lower ($p < 0.01$ by ANOVA) from that on the remaining substrates. It is reported that collagen content, diameters of collagen fibrils and level of collagen cross-linking are higher in adult heart valve compared to that in fetal heart valve.[31] It may be possible that collagen content on the substrates would increase over time as more collagen deposition increases fibril diameter. With more collagen deposition and PCL degradation, the growing construct could be progressively transformed toward more biologic construct. At that time, the construct may bear valve-specific strain. Transmission electron microscopy (TEM) images of these collagen fibrils show the band periodicities confirming type I collagen;[32] however, among the substrates, periodicity in collagen fibrils was most and least distinct on CON and WPD substrates, respectively (Figures 6i−l and Figure S3).

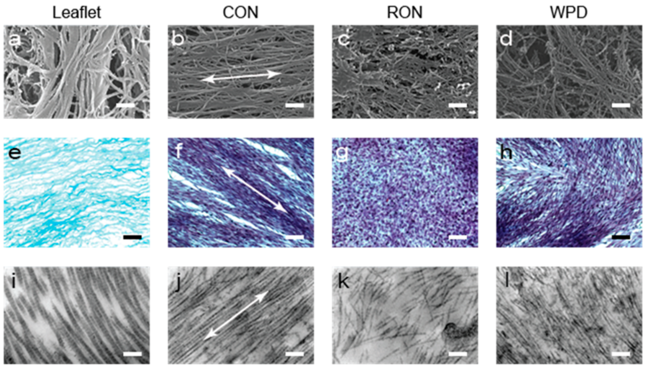

Figure 6. Characteristics of deposited collagen fibrils on substrates and in fibrosa layers of PAV leaflets. (a−d) SEM images of collagen fibrils on various substrates and in a fibrosa layer of a PAV leaflet. Although they were aligned in (a) PAV fibrosa layers and on (b) CON substrates, they were randomly oriented and sparsely aligned on (c) RON and (d) WPD substrates, respectively, scale: 350 nm. (e−h) Masson's trichrome stained collagen fibrils and VICs. Although blue-stained collagen fibrils were highly oriented in (e) PAV fibrosa layers and on (f) CON substrates, they were randomly oriented on (g) RON substrates. On (h) WPD substrates, they had radial orientation sporadically. Red-stained cells (cytoplasm) against blue-stained collagen fibrils brought violet color, scale: 130 μm. (i−l) TEM images of collagen fibrils in a PAV fibrosa layer and on the CON, RON and WPD substrates, respectively. Their band periodicities were most distinct in (i) PAV leaflets and least distinct on (l) WPD substrates. The periodicity on (j) CON substrates was better than that on (k) RON substrates, scale 250 nm. White arrows show the fiber orientation in the CON substrates.

Cross-section images obtained through TEM exhibit a higher number of cell layers with collagen fibrils between the layers of cells on CON and RON substrates than on WPD substrates (Figures 7a−c). The number of layers depended on the thickness of the CON or RON substrates (Figure S2). Thickness of substrates was more than the distance between the cell layers and this phenomenon demonstrated the

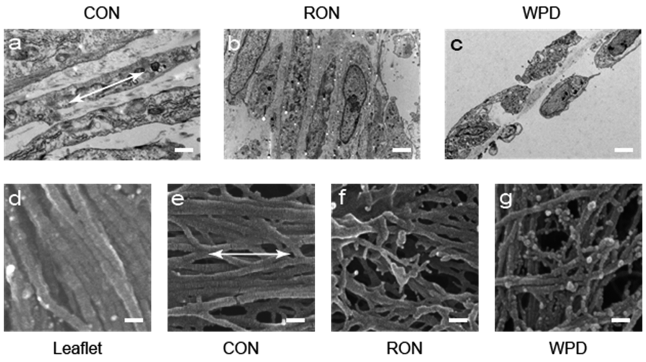

Figure 7. Layered VICs on substrates and surface characteristics of deposited collagen fibrils on them and in fibrosa layers of PAV leaflets. (a−c) TEM images of cell layers and collagen fibrils between the cell layers on CON, RON and WPD substrates. Although there were mostly two cell layers on (c) WPD substrates, more than two cell layers were observed on (a) CON and (b) RON substrates, scale: 3.75 μm. (d−g) Magnified version of SEM images of collagen fibrils mentioned in Figure 2a−d to see the surface smoothness of collagen fibrils. Collagen fibrils in (d) PAV leaflets, on (e) CON substrates, and on (f) RON substrates were smooth but not on (g) WPD substrates, scale: 70 nm. White arrows show the fiber orientation in the CON substrates.

penetration of cells inside the substrates. With fewer cell layers and the lowest fibril diameter, WPD substrates had the highest amount of collagen deposition (2.76 ± 0.34 μg of hydroxyproline/mg).[33] CON and RON substrates and leaflets had a collagen deposition (in terms of hydroxyproline) of 1.73 ± 0.25 μg/mg, 0.23 ± 0.03 μg/mg, and 1.81 ± 0.21 μg/mg, respectively. Collagen deposition on the RON substrate was significantly lower ($p < 0.01$ by ANOVA) than that on the remaining substrates. Higher stiffness of WPD substrates compared to those of CON and RON substrates was responsible for lower fibril diameter and higher fibril density[34] and could lead to higher collagen deposition on WPD substrates.[35]

At higher magnification, the collagen fibrils on CON and RON substrates were very smooth, similar to the collagen fibrils in fibrosa layer of leaflets (Figures 7d−f). In contrast, collagen fibrils on WPD substrates revealed a large number of tiny nodules (size <30 nm) (Figure 7g). However, in their energy-dispersive X-ray (EDX) spectrum,[36] no traces of calcium, sodium, and phosphorus—the elements in hydroxyapatite—were observed on substrates (data not provided). Furthermore, no positive staining was observed in any of the substrate samples in the Alizarin Red S staining assay (ARS, for calcium staining)[37] (Figure S4). TEM imaging also did not show any evidence of electron-dense mineral deposits.

VICs may assume various phenotypes including those of native quiescent fibroblasts, active fibroblasts, active myofibroblasts, and osteoblasts in aortic valve leaflets depending on their surrounding environment and valve status.[38,39] Ratings of gene expression of these phenotypes are listed in Table S1.[38,39] Gene expression from VICs on different substrates and from the whole PAV leaflets was quantified (Figure 8a). VICs on RON substrates had low expression of vimentin and COL1A1 and high expression of α-SMA, which signifies that VICs on RON substrates were similar to the active myofibroblast phenotype.[14,38,40] Also, collagen deposition on this substrate was low.[40] In contrast, VICs on CON substrates had lower expression of α-SMA but higher expression of both vimentin and COL1A1 compared to that on RON substrates; thus, their phenotypes could be consistent with active fibroblasts. This leads to the formation of a model fibrosa layer with increased collagen type I deposition on the CON substrate.[38] VICs in PAV leaflets had little higher expression of vimentin and COL1A1 and lower expression of α-SMA compared to that on CON substrates. Consequently, the phenotype of VICs in PAV leaflets could be active fibroblast. Free edge of PAV leaflets is subjected to dynamic remodeling and can cause the fibroblast to be active leading to α-SMA expression.[41,42] On WPD substrates, VICs had higher expression of all genes and thus represented a highly active myofibroblast phenotype, which is associated with contraction of leaflets, fibrotic stiffening and calcification in the leaflets through their differentiation toward osteoblast-like cells unless the substrate/leaflet is in the development stage.[22,43] To study contraction, we cultured VICs on polystyrene coverslips; within 10 days of culturing, contraction of VICs made all the coverslips bend, whereas fewer RON and almost no CON substrates showed any contraction from VICs after 30 days of culturing (Figure S5). This contraction study on a much stronger coverslip (stiffness ~3 GPa) compared to CON (stiffness ~0.33 MPa) or RON (stiffness ~3.82 MPa) substrate proved that VICs on WPD substrates were beyond development stage. The VICs on WPD substrates had higher expression of COL1A1 compared to VICs

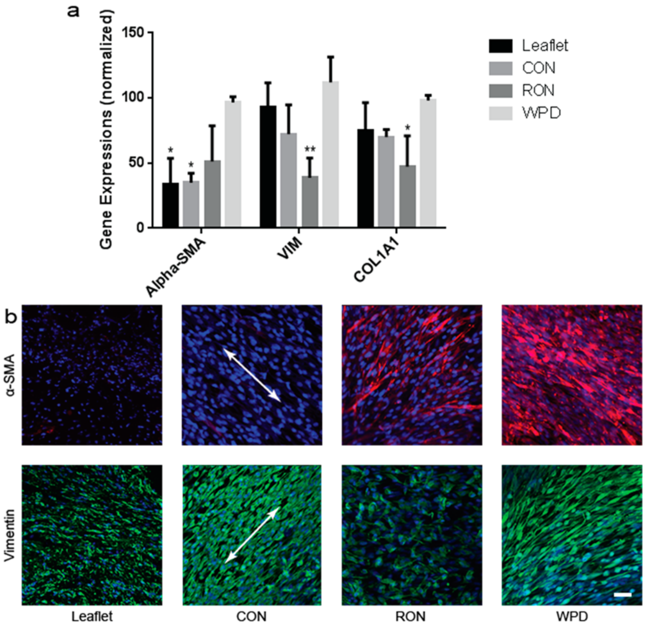

Figure 8. Gene expression and immunostaining analysis of VICs on substrates and in PAV leaflets. (a) Alpha-SMA (α-SMA), VIM (vimentin), and COL1A1 expression of VICs on CON, RON, WPD substrates and in PAV leaflets were compared. Expression of all genes were highest on the WPD substrate. Except for Alpha-SMA, expression of other genes were low on RON substrate. In contrast, except for Alpha-SMA, expression of other genes were high on CON substrate and in leaflet. * and ** denote statistical significance $p < 0.05$ and $p < 0.01$, respectively, as compared with WPD. The results shown are mean values ± SD ($n = 4$). (b) Alpha-SMA and vimentin staining corroborated the gene expression of VICs on CON, RON and WPD substrates, and in PAV leaflets. More positive staining of Alpha-SMA was observed on WPD and RON substrates compared to that on CON substrates and in leaflets. VIM stained VICs also confirmed their orientations found in their SEM images, scale: 27.2 μm. White arrows show the fiber orientation in the CON substrates.

on other substrates, coinciding with higher collagen fibril deposition on WPD substrates.

Because low bulk mechanical properties of CON substrates, VICs demonstrated active fibroblast phenotype (high vimentin, high collagen type I and low α-SMA expression).[38] CON substrates could have been in the developing state or could be near to fully grown because their α-SMA expression was comparatively higher than that of native leaflets without any contraction. However, the same VICs showed myofibroblast phenotype on a substrate (hydrogel, a nonfibrous substrate) with modulus as low as 15 kPa.[14] Nanofibrous morphology of CON substrates could be responsible for the fibroblast phenotype of VICs on the substrates. VICs on RON substrates with higher stiffness (3.82 ± 1.03 MPa) compared to CON substrates had an active myofibroblast phenotype that could lead to a contractile myofibroblast phenotype with the passage of time. Thus, this study brings forth an apparent but important conclusion: although the phenotype of VICs depends mainly on substrate mechanical properties,[44] the substrate morphology also may influence it.

To further confirm protein expression qualitatively, we immunostained VICs from substrates and native PAV leaflets (Figure 8b). VICs on all substrates demonstrated vimentin expression whereas their α-SMA expression varied. VICs on CON substrates had almost no α-SMA staining, whereas α-SMA positive smooth muscle stress fibers were present on RON substrates. Although most of the VICs in leaflets did not express α-SMA, the VICs at the free edge showed α-SMA immunoreactivity (Figure S6). This positive α-SMA staining confirms the α-SMA expression in PAV leaflets. VICs on WPD substrates expressed α-SMA throughout the constructs.

The nature of generated focal adhesions (FAs) of VICs on the underlying substrates may explain the cells' behavior and their phenotype expression.[45,46] The growth, size, maturity and number of FAs depend on morphology, mechanical, and biophysiochemical properties of substrates. Reports indicate that the number of FAs on a planar surface is more than on the substrates made of nanofibers.[47,48] However, more concentrated FA clusters were observed on aligned nanofibers than on flat surfaces when both the nanofiber and the flat surface were made from same material (polymer).[49] Electrospun nanofibers could have higher mechanical properties compared to a flat surface counterpart as the polymer chains in nanofibers are more oriented than in the flat surface.[50] Therefore, compared to morphology, mechanical properties of a substrate could be more responsible for FA cluster formation. Substrates with high mechanical properties show the presence of large supermature FAs (SuFAs) that allow incorporation of α-SMA into preexisting cytoplasmic actin stress fibers leading to myofibroblastic phenotype of fibroblasts.[51] The generated force by α-SMA actin stress fibers is much higher than the force from cytoplasmic actin stress fibers; thus, α-SMA actin stress fibers can cause contraction if the myofibroblastic phenotype continues after tissue development or remodeling. FAs on substrates with less stiffness are less mature and smaller in size, and, in the cells on those substrates, α-SMA does not get into cytoplasmic actin stress fibers. This state could represent the active fibroblast phenotype expression of VICs. Further, more cell−cell contacts on a substrate are in favor of fibroblast phenotype.[52] The above relationship between mechanical properties of a substrate and VICs' FA cluster formation on that substrate could elucidate the cause of different phenotype expression by VICs and their related phenomena on CON, RON, and WPD substrates.

In addition to collagen type I, the elastin deposition by VICs on CON, RON, and WPD substrates were quantified and compared with those obtained from PAV leaflets. Elastin deposition on WPD substrates (56.98 ± 8.04 μg/mg) was greater than that on CON substrates (46.26 ± 7.11 μg/mg), RON substrates (34.12 ± 4.13 μg/mg) and in leaflets (88.30 ± 12.54 μg/mg). To quantify elastin in leaflets, we considered half of a leaflet weight as elastin is found mainly in ventricularis layer and partly in fibrosa layer. Elastin deposition on RON substrate was significantly lower ($p < 0.01$ by ANOVA) from that on other substrates. Higher mechanical properties of the WPD substrates, and especially radial orientation of VICs on that substrate, could be responsible for this higher elastin deposition with respect to CON substrate.

The VICs on the pliable CON substrates showed fibroblast phenotype with circumferential orientation. Further, they demonstrated molecular signature comparable to a leaflet of an aortic valve. In contrast, VICs had an active myofibroblast phenotype with random cell orientation and less deposition of type I collagen on RON substrate compared to that on CON substrate. Therefore, the RON substrates could not mimic the fibrosa layer. WPD substrates were not at all useful in producing an artificial fibrosa layer, as VICs showed a highly active myofibroblast phenotype due to the flat morphology and high mechanical properties of WPD substrates with no guidance to the cells. Thus, VIC-cultured WPD substrates could be inappropriate for valve dysfunction study. Therefore, it can be believed that VIC-cultured CON substrates could have mimicked fibrosa layer in terms of morphology and molecular signature. The VICs were confluent in CON substrate but not in a leaflet. The collagen fibrils in the CON substrates are smaller in diameter than their native counterpart in a leaflet. Thus, it is possible that the fibrosa layer construct with CON substrate was in a growth stage.[29,31] As time passes, more collagen deposition on the CON substrate from VICs would make the substrate stronger and comparable to a native fibrosa layer.[53] A limitation of this study is that gene expression and protein quantification of CON, RON, and WPD samples were compared with those of a whole native leaflet instead of its fibrosa layer. Further, a leaflet is consisted of three layers: circumferentially oriented collagen fiber-based fibrosa layer, randomly oriented proteoglycan-containing spongiosa layer, and radially oriented elastin fiber-rich ventricularis, and in development of native fibrosa layer, other two remaining layers certainly have the effects directly or indirectly.[35] These effects were not available in our in vitro fibrosa development, which may be responsible for low diameter of collagen fibrils, less ECM deposition, higher cell density, etc., in the construct. Our future endeavor to develop a trilayered nanofibrous construct mimicking a leaflet of an aortic heart valve may resolve the issues rose in this study.

■ CONCLUSIONS

In this study, effort was made to develop a prototype of a fibrosa layer of an aortic heart valve through morphology dependent manifestation of VICs. For this purpose, we developed a circumferentially oriented nanofibrous substrate mimicking the morphology of a fibrosa layer of an aortic valve and cultured it with VICs. The VICs and their deposited collagen on the nanofibrous substrate were circumferentially oriented. They demonstrated gene and protein expression close to that of a native aortic leaflet. In contrast, RON and WPD substrates that were applied as control substrates did not show properties conducive to mimicking fibrosa layer morphologically and biologically when cultured with VICs. When applying VICs from human sources, this CON-based prototype can be useful for appropriate in vitro studies of the aortic heart valves.

■ EXPERIMENTAL SECTION

Fabrication of Electrospinning Collector. An aluminum ring of inner diameter and outer diameter 1 and 1.05 in., respectively, and of thickness 0.04 in. was prepared from an aluminum plate. The ring contained 24 equally spaced holes that can fit 24-guage aluminum wire (Malin Co. USA). Twelve aluminum spokes were made from aluminum wire and placed in the opposite holes of the aluminum ring to prepare metallic spoke-in-ring collector.

Fabrication of PCL Ring-Frame. One side of the metal ring intended to prepare the circumferentially or randomly oriented nanofibrous layer was coated with biocompatible grease. An 18% (wt/v) polycaprolactone (PCL, MW: 80 KD, Sigma-Aldrich, USA) solution in trifluoroethanol (Sigma-Aldrich, USA) was poured on that side to make a PCL ring-frame attached to the metal ring. The thickness of the PCL ring-frame was ∼0.25 mm.

Fabrication of Substrate. A 9% (wt/v) polycaprolactone (PCL, MW: 80 KD, Sigma-Aldrich, USA) solution in trifluoroethanol (Sigma-Aldrich, USA) was electrospun at a discharge rate of 0.3 mL/h, with a gap distance between spinneret needle (blunt point, 18-gauge diameter and 2-in. length) and collector of 22 cm and at a voltage supply of 16 kV to produce PCL nanofibers. An aluminum spoke-in-ring collector was used to fabricate concentrically oriented nanofibrous (CON) substrates. The ring without spokes was placed on the metal plate to produce randomly oriented nanofibrous (RON) substrates. One side of the collector was coated with a layer of PCL before electrospinning so that the nanofibrous structures can function as standalone substrates individually after being detached from the collectors. A 1 in. disc cut from the bottom of wells of polystyrene 6-well tissue culture plate was used as another type of control substrate (WPD substrate).

Tensile Testing. A Microscale tensile tester (Bose Electroforce, USA) was used for uniaxial tensile testing of both aligned and randomly oriented substrates. A third of a sample was sandwiched between two paper window frames with a window dimension of 11 mm × 10 mm to prepare the test sample. Test samples were loaded at the extension rate 0.1 mm/s. A 150 g load cell was used to sense the load on samples until failure. Circumferentially oriented nanofibrous samples were pulled in the circumferential direction. Randomly oriented samples were pulled along the test direction. The thickness of the samples was measured using their SEM images. The tensile properties of WPD substrate were obtained from data reported in the literature.[14]

Straight aligned nanofibers were electrospun between two parallel metal plates, collected and then sandwiched between two paper window frames for their tensile tests along the aligned nanofibers.

Cell Extraction and Culture. Aortic valve leaflets were aseptically collected from pig hearts obtained from Hormel Foods (Austin, MN, USA), washed in a copious amount of sterile PBS and placed in trypsin (Invitrogen, USA) at 37 °C for 5 min. The leaflets were then swabbed gently to remove the endothelial layer from their surfaces and then digested in 0.5% (wt/v) type I collagenase (Worthington Biochemical, USA) in PBS at 37 °C for 5 h. VICs were then isolated by centrifuging the digestion at 1000 rpm for 10 min and resuspended and expanded in tissue culture (TC) media from Dulbecco's modified Eagle's medium (DMEM, Corning, USA) supplemented with 10% fetal bovine serum (FBS), Atlas Biologicals, USA) and 1% penicillin-streptomycin (Life Technologies, USA).

Cell Seeding and Culture. The CON, RON and WPD substrates were sterilized by incubating them in 70% ethanol for 1 h at room temperature (25 °C) and then washing in a copious amount of phosphate buffer saline (PBS), Hyclone, USA) in a sterile place. We seeded 1 million VICs in 2 mL of TC media with ascorbic acid (150 μg/mL) (TC-A media) on nanofibrous samples. After the first day of culture, close to 100 000 cells had attached to nanofibers in each of the CON and RON substrates, and 100 000 VICs were seeded on the WPD substrate. The seeded cells on those substrates were cultured in TC-A media for one month with replenishing of the media every 3 days.

Cell Proliferation Study. We used the AlamarBlue (AB, Invitrogen, USA) calorimetric assay to study the VIC proliferation on three types of substrates with the passage of time, following the company protocol. Briefly, samples were washed in PBS and incubated in 10% AB solution in TC media in a tissue culture incubator. We transferred 200 μL of the assay solution to a 96-well plate in triplicate and measured at 560 nm (absorbance) in a spectrophotometer (SpectraMax Plus 384, Molecular Devices, USA). The measured absorbance data were transformed to cell numbers using a calibrated curve produced from the absorbance data of known cell numbers. Cell numbers were counted at 1, 3, 11, and 21-day time points.

SEM Imaging. Transverse and fibrosa layer sections were cut from frozen PAV leaflet tissue samples in OCT in a microtome. Tissue sections and cultured samples were fixed in 4% formaldehyde overnight at 4 °C. The samples were then rinsed in PBS, dehydrated in a graded ethanol series and dried in a critical point drier. Dried samples including plain substrates were sputter coated with gold—palladium at 18 mA for 20 s and imaged with a scanning electron microscope (Hitachi, Japan) with a EDX detector (Carl Zeiss, USA).

TEM Imaging. Samples were fixed in a mixture of 2.5% glutaraldehyde and 4% formaldehyde in PBS for 2 h, rinsed in PBS, fixed in 1% osmium tetroxide for 1 h, washed in distilled water, and then dehydrated through graded ethanol. For epoxy resin infiltration, the samples were treated with an ethanol—acetone mixture (1:1, by volume) for 10 min, acetone for 10 min, acetone—epoxy resin (2:1, by volume) for 30 min, acetone—epoxy resin (1:1, by volume) for 30 min, acetone—epoxy resin (1:2, by volume) for 30 min, and epoxy resin overnight. The samples were then embedded in fresh epoxy resin and cured overnight at 60 °C. The embedded samples were sectioned, collected on a copper grid, and imaged with transmission electron microscopy (Jeol, Japan).

Protein Quantification. For collagen quantifications, cultures and leaflet samples were rinsed in PBS and lyophilized. Their weights were measured and they were digested in papainase buffer containing papain type III (Worthington Biochemical, USA). Supernatants were collected by centrifugation for collagen quantifications performed according to manufacturer protocol (Sigma, USA). In brief, 100 μL of the papain digest was added to 100 μL of 12 N HCl and hydrolyzed at 120 °C for 3 h. We transferred 50 μL of the hydrolyzed sample to a 96-well plate and dried it at 60 °C. A 100 μL chloramine T/oxidation buffer mixture (94:6) was added to the dried sample and incubated at room temp for 5 min; then 100 μL of diluted DAMB reagent was added to the sample and incubated at 60 °C for 90 min. After cooling the samples to room temperature, we recorded their absorbance at 557 nm and compared with standard curve obtained by measuring the absorbance of known hydroxyproline solution.

Elastin was quantified according to company protocol (Fastin, Biocolor, USA). Cultures and leaflet samples were rinsed in PBS and lyophilized. They were weighed and then incubated in 0.25 M oxalic acid at 100 °C for 1 h. After centrifuging, the supernatant was added to elastin precipitate agent and the precipitate was dyed with dying agent through complete mixing. Through centrifuging, dyed elation was collected as precipitate and then dissociated with an agent. The sample was then analyzed at 513 nm absorbance and compared with standard curve obtained by measuring the absorbance of known elastin standard solutions.

Gene Expression Analysis. RNA from cultured samples and whole leaflet samples was extracted using a Pure Link RNA mini kit (Ambion, Life Technologies, USA) according to manufacturer's protocol with little modification. The cultured samples were washed with PBS, snap freezed in liquid nitrogen and kept at −80 °C until all the samples were collected. The frozen samples were homogenized instantly (thawing occurred at this point) in lysis buffer. The homogenized solutions were processed according to protocol to extract RNA. The extracted RNA was purified with DNase I (Life Technologies, USA) according to manufacturer's protocol. First-strand cDNA was synthesized from purified RNA using High-Capacity cDNA Reverse Transcription kit with RNase Inhibitor (Applied Biosystems, USA). cDNA transcripts were then probed with TaqMan assays for vimentin (Ss04330801_gH), α-smooth muscle actin (α-SMA, Ss04245588_m1), and type I collagen (COL1A1, Ss03373341_g1) using Lightcycler 480 Probe master mix (Roche, USA). Thermocycling was performed in a Lightcycler 480 (Roche Applied Science, USA) with the following conditions: preincubation (95 °C, 15 min), 40 cycles of amplification (denaturation: 95 °C, 15 s; annealing: 60 °C, 1 min; and extension: 72 °C, 1 s) and cooling (40 °C, 30 s). Target gene data were normalized against ACTB level and analyzed using the comparative cycle threshold (Ct) method.

Masson's Trichrome Staining. Fibrosa layer sections were cut from frozen PAV leaflet tissue samples in OCT in a microtome. Tissue sections and cultured samples were fixed in 4% formaldehyde overnight at 4 °C. The samples were then rinsed in PBS and then stained with Masson's trichrome using manufacturer's instruction (Sigma-Aldrich, USA). The samples were then rinsed, dehydrated, mounted on glass slides using a mounting media, and imaged in an optical microscope.

Alizarin Staining. Fibrosa layer sections were cut from frozen PAV leaflet tissue samples in OCT in a microtome. Tissue sections and cultured samples were fixed in 4% formaldehyde overnight at 4 °C. They were then treated with 2 wt/v% alizarin Red S (Sigma-Aldrich, USA) solution (pH 4.1–4.3) for 10 min, washed with DI water and then viewed through an optical microscope.

Immunostaining. Fibrosa layer sections were cut from frozen PAV leaflet tissue samples in OCT in a microtome. Tissue sections and cultured samples were fixed in 4% methanol-free formaldehyde overnight at 4 °C. The samples were washed in PBS, incubated in 0.1% Triton X-100 for 2 min, washed in PBS, and incubated in 10% goat serum for 30 min. The samples were then incubated in a mouse antivimentin IgM primary antibody (Novus Biologicals, USA) at a 1:500 dilution in PBS for 1 h. They were then washed in PBS and incubated in AF 488 conjugated goat antimouse IgM secondary antibody (Abcam, USA) at 1:500 dilution in PBS for 45 min. The samples were then washed in PBS and mounted on glass slide using Prolong Gold Antifade reagent with DAPI (Invitrogen) mounting media. For smooth muscle actin staining, primary and secondary antibodies were mouse antihuman smooth muscle actin IgG (Dako, USA) and AF 594 conjugated goat antimouse IgG (Abcam, USA). The stained samples were imaged through a confocal microscopy.

Statistical Analysis. Data are reported as mean ± standard deviation (SD). Data were compared using one-way ANOVA followed by Duncan's posthoc tests for statistical significance through GraphPad Prism software. P values <0.05 were considered to indicate significance (*$p < 0.05$ and **$p < 0.01$).

■ ASSOCIATED CONTENT

Ⓢ Supporting Information

The Supporting Information is available free of charge on the ACS Publications website at DOI: 10.1021/acsami.5b04805.

Figures S1–S6 and Table S1 (PDF)

■ AUTHOR INFORMATION

Corresponding Authors

*E-mail: Lerman.Amir@mayo.edu. Phone: 507-284-3727. Fax: 507-538-6418.
*E-mail: rsimari@kumc.edu Phone: 913-588-7201 Fax: 913-588-7235.

Notes

The authors declare the following competing financial interest(s): Authors filed a Provisional Patent Application (US patent application No. 62/15488, filed April 30, 2015).

■ ACKNOWLEDGMENTS

The authors thank Federico Franchi, PhD, for help with RT-PCR assay and Tyra Witt for sample sectioning. This work is supported by the HH Sheikh Hamed bin Zayed Al Nahyan Program in Biological Valve Engineering, the Grainger Foundation (94381008), and the Mayo Clinic Center for Regenerative Medicine.

■ REFERENCES

(1) The Lancet staff. Cardiovascular health crisis. *Lancet* **2010**, *376*, 1874–1874.

(2) *Promoting Cardiovascular Health in the Developing World: A Critical Challenge to Achieve Global Health*; Fuster, V., Kelly, B. B., Eds.; National Academies Press: Washington, D.C., 2010; p 484.

(3) Jana, S.; Simari, R. D.; Spoon, D. B.; Lerman, A. Drug Delivery in Aortic Valve Tissue Engineering. *J. Controlled Release* **2014**, *196*, 307–323.

(4) Jana, S.; Tranquillo, R. T.; Lerman, A. Cells for Tissue Engineering of Cardiac Valves. *J. Tissue Eng. Regener. Med.* **2015**, DOI: 10.1002/term.2010.

(5) Leopold, J. A. Cellular Mechanisms of Aortic Valve Calcification. *Circ.: Cardiovasc. Interventions* **2012**, *5*, 605–614.

(6) Staico, R.; Armaganijan, L.; Lopes, R. D. Coronary Embolism and Calcified Aortic Valve: Is There a Correlation? *J. Thromb. Thrombolysis* **2012**, *34*, 425–427.

(7) Freeman, R. V.; Otto, C. M. Spectrum of Calcific Aortic Valve Disease: Pathogenesis, Disease Progression, and Treatment Strategies. *Circulation* **2005**, *111*, 3316–3326.

(8) Furukawa, K. Recent advances in research on human aortic valve calcification. *J. Pharmacol. Sci.* **2014**, *124*, 129–137.

(9) Butcher, J. T.; Nerem, R. M. Valvular Endothelial Cells Regulate the Phenotype of Interstitial Cells in Co-culture: Effects of Steady Shear Stress. *Tissue Eng.* **2006**, *12*, 905–915.

(10) Liu, A. C.; Joag, V. R.; Gotlieb, A. I. The Emerging Role of Valve Interstitial Cell Phenotypes in Regulating Heart Valve Pathobiology. *Am. J. Pathol.* **2007**, *171*, 1407–1418.

(11) Paranya, G.; Vineberg, S.; Dvorin, E.; Kaushal, S.; Roth, S. J.; Rabkin, E.; Schoen, F. J.; Bischoff, J. Aortic Valve Endothelial Cells Undergo Transforming Growth Factor-beta-mediated and Non-transforming Growth Factor-beta-mediated Transdifferentiation in Vitro. *Am. J. Pathol.* **2001**, *159*, 1335–1343.

(12) Wang, H. S.; Hung, S. C.; Peng, S. T.; Huang, C. C.; Wei, H. M.; Guo, Y. J.; Fu, Y. S.; Lai, M. C.; Chen, C. C. Mesenchymal Stem Cells in the Wharton's Jelly of the Human Umbilical Cord. *Stem Cells* **2004**, *22*, 1330–1337.

(13) Stella, J. A.; Sacks, M. S. On the Biaxial Mechanical Properties of the Layers of the Aortic Valve Leaflet. *J. Biomech. Eng.* **2007**, *129*, 757–766.

(14) Wang, H.; Tibbitt, M. W.; Langer, S. J.; Leinwand, L. A.; Anseth, K. S. Hydrogels Preserve Native Phenotypes of Valvular Fibroblasts Through an Elasticity-regulated PI3K/AKT Pathway. *Proc. Natl. Acad. Sci. U. S. A.* **2013**, *110*, 19336–19341.

(15) Jana, S.; Cooper, A.; Ohuchi, F.; Zhang, M. Q. Uniaxially Aligned Nanofibrous Cylinders by Electrospinning. *ACS Appl. Mater. Interfaces* **2012**, *4*, 4817–4824.

(16) Jana, S.; Leung, M.; Chang, J.; Zhang, M. Effect of Nano- and Micro-scale Topological Features on Alignment of Muscle Cells and Commitment of Myogenic Differentiation. *Biofabrication* **2014**, *6*, 035012.

(17) Jana, S.; Zhang, M. Fabrication of 3D Aligned Nanofibrous Tubes by Direct Electrospinning. *J. Mater. Chem. B* **2013**, *1*, 2575–2581.

(18) Woodruff, M. A.; Hutmacher, D. W. The Return of a Forgotten Polymer—Polycaprolactone in the 21st Century. *Prog. Polym. Sci.* **2010**, *35*, 1217–1256.

(19) Kievit, F. M.; Cooper, A.; Jana, S.; Leung, M. C.; Wang, K.; Edmondson, D.; Wood, D.; Lee, J. S.; Ellenbogen, R. G.; Zhang, M. Aligned Chitosan-Polycaprolactone Polyblend Nanofibers Promote

the Migration of Glioblastoma Cells. *Adv. Healthcare Mater.* **2013**, *2*, 1651−1659.

(20) Leung, M.; Jana, S.; Tsao, C.-T.; Zhang, M. TEnogenic Differentiation of Human Bone Marrow Stem Cells via a Combinatory Effect of Aligned Chitosan-poly-caprolactone Nanofibers and TGF-[Small Beta]3. *J. Mater. Chem. B* **2013**, *1*, 6516−6524.

(21) Diaz, E.; Sandonis, I.; Valle, M. B. In Vitro Degradation of Poly(caprolactone)/nHA Composites. *J. Nanomater.* **2014**, *2014*, 1−8.

(22) Masoumi, N.; Annabi, N.; Assmann, A.; Larson, B. L.; Hjortnaes, J.; Alemdar, N.; Kharaziha, M.; Manning, K. B.; Mayer, J. E., Jr.; Khademhosseini, A. Tri-layered Elastomeric Scaffolds for Engineering Heart Valve Leaflets. *Biomaterials* **2014**, *35*, 7774−7785.

(23) Rouabah, F.; Dadache, D.; Haddaoui, N. Thermophysical and Mechanical Properties of Polystyrene: Influence of Free Quenching. *ISRN Polym. Sci.* **2012**, *2012*, 161364.

(24) Tan, A. J.; Holt, D. L. The Effects of Sterilization and Storage Treatments on the Stress-strain Behavior of Aortic Valve Leaflets. *Ann. Thorac. Surg.* **1976**, *22*, 188−194.

(25) Billiar, K. L.; Sacks, M. S. Biaxial Mechanical Properties of the Natural and Glutaraldehyde Treated Aortic Valve Cusp−part I: Experimental Results. *J. Biomech. Eng.* **2000**, *122*, 23−30.

(26) Walker, G. A.; Masters, K. S.; Shah, D. N.; Anseth, K. S.; Leinwand, L. A. Valvular Myofibroblast Activation by Transforming Growth Factor-beta: Implications for Pathological Extracellular Matrix Remodeling in Heart Valve Disease. *Circ. Res.* **2004**, *95*, 253−260.

(27) Weiss, R. M.; Miller, J. D.; Heistad, D. D. Fibrocalcific Aortic Valve Disease: Opportunity to Understand Disease Mechanisms Using Mouse Models. *Circ. Res.* **2013**, *113*, 209−222.

(28) Syedain, Z. H.; Bradee, A. R.; Kren, S.; Taylor, D. A.; Tranquillo, R. T. Decellularized Tissue-engineered Heart Valve Leaflets with Recellularization Potential. *Tissue Eng., Part A* **2013**, *19*, 759−769.

(29) Aikawa, E.; Whittaker, P.; Farber, M.; Mendelson, K.; Padera, R. F.; Aikawa, M.; Schoen, F. J. Human Semilunar Cardiac Valve Remodeling by Activated Cells from Fetus to Adult: Implications for Postnatal Adaptation, Pathology, and Tissue Engineering. *Circulation* **2006**, *113*, 1344−1352.

(30) Cuerrier, C. M.; Chen, Y. X.; Tremblay, D.; Rayner, K.; McNulty, M.; Zhao, X.; Kennedy, C. R.; de BelleRoche, J.; Pelling, A. E.; O'Brien, E. R. Chronic Over-expression of Heat Shock Protein 27 Attenuates Atherogenesis and Enhances Plaque Remodeling: a Combined Histological and Mechanical Assessment of Aortic Lesions. *PLoS One* **2013**, *8*, e55867.

(31) Kasyanov, V.; Moreno-Rodriguez, R. A.; Kalejs, M.; Ozolanta, I.; Stradins, P.; Wen, X.; Yao, H.; Mironov, V. Age-related Analysis of Structural, Biochemical and Mechanical Properties of the Porcine Mitral Heart Valve Leaflets. *Connect. Tissue Res.* **2013**, *54*, 394−402.

(32) Starborg, T.; Lu, Y.; Meadows, R. S.; Kadler, K. E.; Holmes, D. F. Electron Microscopy in Cell-matrix Research. *Methods (Amsterdam, Neth.)* **2008**, *45*, 53−64.

(33) Zhan, J.; Singh, A.; Zhang, Z.; Huang, L.; Elisseeff, J. H. Multifunctional Aliphatic Polyester Nanofibers for Tissue Engineering. *Biomatter* **2012**, *2*, 202−212.

(34) Balguid, A.; Driessen, N. J.; Mol, A.; Schmitz, J. P.; Verheyen, F.; Bouten, C. V.; Baaijens, F. P. Stress Related Collagen Ultrastructure in Human Aortic Valves−implications for Tissue Engineering. *J. Biomech.* **2008**, *41*, 2612−2617.

(35) Jana, S.; Tefft, B. J.; Spoon, D. B.; Simari, R. D. Scaffolds for Tissue Engineering of Cardiac Valves. *Acta Biomater.* **2014**, *10*, 2877−2893.

(36) Bertazzo, S.; Gentleman, E.; Cloyd, K. L.; Chester, A. H.; Yacoub, M. H.; Stevens, M. M. Nano-analytical Electron Microscopy Reveals Fundamental Insights into Human Cardiovascular Tissue Calcification. *Nat. Mater.* **2013**, *12*, 576−583.

(37) Leroux-Berger, M.; Queguiner, I.; Maciel, T. T.; Ho, A.; Relaix, F.; Kempf, H. Pathologic Calcification of Adult Vascular Smooth Muscle Cells Differs on Their Crest or Mesodermal Embryonic Origin. *J. Bone Miner. Res.* **2011**, *26*, 1543−1553.

(38) Akamatsu, T.; Arai, Y.; Kosugi, I.; Kawasaki, H.; Meguro, S.; Sakao, M.; Shibata, K.; Suda, T.; Chida, K.; Iwashita, T. Direct Isolation of Myofibroblasts and Fibroblasts from Bleomycin-injured Lungs Reveals Their Functional Similarities and Differences. *Fibrog. Tissue Repair* **2013**, *6*, 1−17.

(39) Thayer, P.; Balachandran, K.; Rathan, S.; Yap, C. H.; Arjunon, S.; Jo, H.; Yoganathan, A. P. The Effects of Combined Cyclic Stretch and Pressure on the Aortic Valve Interstitial Cell Phenotype. *Ann. Biomed. Eng.* **2011**, *39*, 1654−1667.

(40) Ricupero, D. A.; Poliks, C. F.; Rishikof, D. C.; Kuang, P. P.; Goldstein, R. H. Apigenin Decreases Expression of the Myofibroblast Phenotype. *FEBS Lett.* **2001**, *506*, 15−21.

(41) Bertipaglia, B.; Ortolani, F.; Petrelli, L.; Gerosa, G.; Spina, M.; Pauletto, P.; Casarotto, D.; Marchini, M.; Sartore, S. Cell Characterization of Porcine Aortic Valve and Decellularized Leaflets Repopulated with Aortic Valve Interstitial Cells: the Vesalio Project (Vitalitate Exornatum Succedaneum Aorticum Labore Ingenioso Obtenibitur). *Ann. Thorac. Surg.* **2003**, *75*, 1274−1282.

(42) Della Rocca, F.; Sartore, S.; Guidolin, D.; Bertiplaglia, B.; Gerosa, G.; Casarotto, D.; Pauletto, P. Cell Composition of the Human Pulmonary Valve: a Comparative Study with the Aortic Valve−the Vesalio Project. Vitalitate Exornatum Succedaneum Aorticum Labore Ingegnoso Obtinebitur. *Ann. Thorac. Surg.* **2000**, *70*, 1594−1600.

(43) Rajamannan, N. M.; Evans, F. J.; Aikawa, E.; Grande-Allen, K. J.; Demer, L. L.; Heistad, D. D.; Simmons, C. A.; Masters, K. S.; Mathieu, P.; O'Brien, K. D.; Schoen, F. J.; Towler, D. A.; Yoganathan, A. P.; Otto, C. M. Calcific Aortic Valve Disease: Not Simply a Degenerative Process: a Review and Agenda for Research from the National Heart and Lung and Blood Institute Aortic Stenosis Working Group. Executive Summary: Calcific Aortic Valve Disease-2011 Update. *Circulation* **2011**, *124*, 1783−1791.

(44) Hinderer, S.; Seifert, J.; Votteler, M.; Shen, N.; Rheinlaender, J.; Schaffer, T. E.; Schenke-Layland, K. Engineering of a Bio-functionalized Hybrid Off-the-shelf Heart Valve. *Biomaterials* **2014**, *35*, 2130−2139.

(45) Sheets, K.; Wang, J.; Meehan, S.; Sharma, P.; Ng, C.; Khan, M.; Koons, B.; Behkam, B.; Nain, A. S. Cell-fiber Interactions on Aligned and Suspended Nanofiber Scaffolds. *J. Biomater. Tissue Eng.* **2013**, *3*, 355−368.

(46) Cukierman, E.; Pankov, R.; Yamada, K. M. Cell Interactions with Three-dimensional Matrices. *Curr. Opin. Cell Biol.* **2002**, *14*, 633−639.

(47) Biggs, M. J.; Richards, R. G.; Gadegaard, N.; Wilkinson, C. D.; Oreffo, R. O.; Dalby, M. J. The Use of Nanoscale Topography to Modulate the Dynamics of Adhesion Formation in Primary Osteoblasts and Erk/mapk Signalling in Stro-1+ Enriched Skeletal Stem Cells. *Biomaterials* **2009**, *30*, 5094−5103.

(48) Sequeira, S. J.; Soscia, D. A.; Oztan, B.; Mosier, A. P.; Jean-Gilles, R.; Gadre, A.; Cady, N. C.; Yener, B.; Castracane, J.; Larsen, M. The Regulation of Focal Adhesion Complex Formation and Salivary Gland Epithelial Cell Organization by Nanofibrous PLGA Scaffolds. *Biomaterials* **2012**, *33*, 3175−3186.

(49) Sheets, K.; Wunsch, S.; Ng, C.; Nain, A. S. Shape-dependent Cell Migration and Focal Adhesion Organization on Suspended and Aligned Nanofiber Scaffolds. *Acta Biomater.* **2013**, *9*, 7169−7177.

(50) Yao, J.; Bastiaansen, C. W. M.; Peijs, T. High Strength and High Modulus Electrospun Nanofibers. *Fibers* **2014**, *2*, 158−187.

(51) Goffin, J. M.; Pittet, P.; Csucs, G.; Lussi, J. W.; Meister, J. J.; Hinz, B. Focal Adhesion Size Controls Tension-dependent Recruitment of Alpha-smooth Muscle Actin to Stress Fibers. *J. Cell Biol.* **2006**, *172*, 259−268.

(52) Hinz, B. Formation and Function of the Myofibroblast During Tissue Repair. *J. Invest. Dermatol.* **2007**, *127*, 526−537.

(53) Nakayama, Y.; Takewa, Y.; Sumikura, H.; Yamanami, M.; Matsui, Y.; Oie, T.; Kishimoto, Y.; Arakawa, M.; Ohmuma, K.; Tajikawa, T.; Kanda, K.; Tatsumi, E. In-body Tissue-engineered Aortic Valve (Biovalve Type VII) Architecture Based on 3D Printer Molding. *J. Biomed. Mater. Res., Part B* **2015**, *103*, 1−11.

DOI: 10.1021/acsami.5b04805
ACS Appl. Mater. Interfaces 2015, 7, 20012−20020